



HAL
open science

Ring dynamics around non-axisymmetric bodies with application to Chariklo and Haumea

B. Sicardy, R. Leiva, S. Renner, F. Roques, M. El Moutamid, P. Santos-Sanz, J. Desmars

► **To cite this version:**

B. Sicardy, R. Leiva, S. Renner, F. Roques, M. El Moutamid, et al.. Ring dynamics around non-axisymmetric bodies with application to Chariklo and Haumea. *Nature Astronomy*, 2019, 3 (2), pp.146-153. 10.1038/s41550-018-0616-8 . hal-02313812

HAL Id: hal-02313812

<https://hal.sorbonne-universite.fr/hal-02313812>

Submitted on 11 Oct 2019

HAL is a multi-disciplinary open access archive for the deposit and dissemination of scientific research documents, whether they are published or not. The documents may come from teaching and research institutions in France or abroad, or from public or private research centers.

L'archive ouverte pluridisciplinaire **HAL**, est destinée au dépôt et à la diffusion de documents scientifiques de niveau recherche, publiés ou non, émanant des établissements d'enseignement et de recherche français ou étrangers, des laboratoires publics ou privés.

Ring dynamics around non-axisymmetric bodies with application to Chariklo and Haumea

B. Sicardy^{*,1}, R. Leiva², S. Renner³, F. Roques¹, M. El Moutamid^{4,5}, P. Santos-Sanz⁶, J. Desmars¹ [This is a pre-print of an article published in *Nature Astronomy*. The final authenticated version is available inline at <http://dx.doi.org/10.1038/s41550-018-0616-8>]

¹LESIA, Observatoire de Paris, Université PSL, CNRS, UPMC, Sorbonne Université, Univ. Paris Diderot, Sorbonne Paris Cité, 5 place Jules Janssen, 92195 Meudon, France ²Southwest Research Institute, Dept. of Space Studies, 1050 Walnut Street, Suite 300, Boulder, CO 80302, USA. ³IMCCE, Observatoire de Paris, CNRS UMR 8028, Université de Lille, Observatoire de Lille, 1, impasse de l'Observatoire, F-59000 Lille, France. ⁴Center for Astrophysics and Planetary Science, Cornell University, Ithaca, NY 14853, USA. ⁵Carl Sagan Institute, Cornell University, Ithaca, NY 14853, USA. ⁶Instituto de Astrofísica de Andalucía (CSIC), Glorieta de la Astronomía S/N, 18008-Granada, Spain.

Dense and narrow rings have been discovered recently around the small Centaur object Chariklo¹ and the dwarf planet Haumea², while being suspected around the Centaur Chiron³, although this point is debated⁴. They are the first rings observed in the Solar System elsewhere than around giant planets. Contrarily to the latter, gravitational fields of small bodies may exhibit large non-axisymmetric terms that create strong resonances between the spin of the object and the mean motion of rings particles. Here we show that modest topographic features or elongations of Chariklo and Haumea explain why their rings are relatively far away from the central body, when scaled to those of the giant planets⁵. Resonances actually clear on decadal time-scales an initial collisional disk that straddles the corotation resonance (where the particles mean motion matches the spin rate of the body). Quite generically, the disk material inside the corotation radius migrates onto the body, while the material outside the corotation radius is pushed outside the 1/2 resonance, where the particles complete one revolution while the body completes two rotations. Consequently, the existence of rings around non-axisymmetric bodies requires that the 1/2 resonance resides inside the Roche limit of the body, favoring faster rotators for being surrounded by rings.

Chariklo and Haumea's non-axisymmetric gravity fields raise new and rich dynamical issues that are not encountered for rings around the giant planets. The strong coupling between the body and the surrounding collisional disk put tight constraints on the ring final location. This is the main topic of this paper, while the possible formation scenarios for those rings, that are discussed elsewhere^{1, 2, 6-11}, will not be addressed here.

To be more specific, Haumea is a triaxial ellipsoid with principal semi-axes $A > B > C$ and elongation $\epsilon \sim 0.61$ (see Table 1). Chariklo's shape is less constrained due to scarce observations. Extreme solutions¹² are a spherical Chariklo of radius $R_{\text{sph}} = 129$ km with topographic features of typical heights $z \sim 5$ km, or an ellipsoid with elongation $\epsilon \sim 0.20$. The two bulges associated with those elongations contain large masses (of order ϵ) compared to the body itself. Even a 5-km topographic feature on Chariklo represents a mass anomaly $\mu \sim (z/2R_{\text{sph}})^3 \sim 10^{-5}$ relative to the body. This is much larger than the mass of Janus (a small satellite that confines the outer edge of Saturn's main rings) with $\mu \sim 3 \times 10^{-9}$, or putative Saturnian mass anomalies¹³, with $\mu < 10^{-12}$, supporting the strong coupling mentioned earlier.

Fig. 1 outlines two possible configurations of Chariklo's dynamical environment, one with a

mass anomaly and one with an elongated body. In both cases, there are four fixed points C_1, \dots, C_4 near the corotation radius $a_{\text{cor}} \sim (GM/\Omega^2)^{1/3} = R/q^{1/3}$, where the dimensionless rotation parameter q is defined by

$$q = \frac{\Omega^2 R^3}{GM}, \quad (1)$$

G being the gravitation constant, M the mass of the body, Ω its spin rate, and R denoting either the radius R_{sph} of a sphere or the reference radius of the ellipsoid (Table 1).

In principle, the region around C_2 or C_4 may host ring arcs, but these points being potential maxima, arcs are unstable against dissipative collisions over time scales of some 10^4 years at most. Moreover, for Chariklo's elongations larger than the critical value $\epsilon_{\text{crit}} \sim 0.16$ (which is the case here with the adopted value $\epsilon = 0.20$), the points C_2 and C_4 are linearly unstable (see Methods). Consequently, particles moving away from C_2 or C_4 rapidly collide with the body (Fig. 1). This problem is exacerbated in the case Haumea, because of its larger elongation, $\epsilon \sim 0.61$.

Particles with mean motion n and epicyclic frequency κ experience Lindblad Resonances (LRs) for

$$\kappa = m(n - \Omega), \quad m \text{ integer}. \quad (2)$$

The resonances occur either inside ($m > 1$) or outside ($m < 0$) the corotation radius (Fig. 1), with only even values of m allowed in the ellipsoid case, due to symmetry reasons (Methods). Only disks revolving in a prograde direction are considered here. Retrograde resonances are weaker¹⁴ and will not be studied here. Since $\kappa \sim n$, the relation above reads $n/\Omega \sim m/(m-1)$, referred to as an $m/(m-1)$ LR. In a disk dense enough to support collective effects (self-gravity, pressure or viscosity), an $m/(m-1)$ LR forces a m -armed spiral wave that receives a torque

$$\Gamma_m = \text{sign}(\Omega - n) \left(\frac{4\pi^2 \Sigma_0}{3n} \right) \frac{(GM)^2}{\Omega R^2} \mathcal{A}_m^2. \quad (3)$$

This formula encapsulates in separate factors the sign of the torque, the physical parameters of the disk (n and its surface density Σ_0) and of the perturber (M , R , Ω), and an intrinsic dimensionless strength factor \mathcal{A}_m , see Methods. Importantly, this is a generic formula that applies in contexts as different as galactic dynamics^{15,16}, circum-stellar accretion disks¹⁷, proto-planetary disks¹⁸ or planetary rings and interiors¹⁹⁻²¹. Moreover, both the sign of the torque and its value are largely independent of the physics of the disk²⁰, providing a robust estimation of Γ_m even ignoring the detailed processes at work.

Eq. (3) shows that the LR causes the migration of the disk material away from the corotation. An annulus of width W and average radius a has most of its angular momentum $H \sim 2\pi a W \Sigma_0 \sqrt{GMa} = 2\pi \Sigma_0 W (\Omega R^3/q)$ transferred to the body over a migration time scale

$$t_{\text{mig}} \sim \frac{H}{|\sum \Gamma_m|} = \frac{3q}{4\pi^2} \left(\frac{W}{R} \right) \left(\frac{T_{\text{rot}}}{\sum [(m-1)/m] \mathcal{A}_m^2} \right), \quad (4)$$

where $T_{\text{rot}} = 2\pi/\Omega$ is the rotation period of the body. The summation includes the relevant torques Γ_m that apply inside the annulus (Fig. 2). Note that the current angular momentum of Chariklo's rings is less than 10^{-5} of that of the body^{1,6}. Even considering an initial disk one hundred times more massive, the reaction torque of the disk on the body has a negligible effect on Chariklo's rotation rate, with similar conclusions for Haumea.

We estimate t_{mig} for two annuli around Chariklo, one initially placed inside the corotation radius, and one placed outside. Fig. 2 shows that (i) a difference $A-B$ as small as a kilometer ($\epsilon \lesssim 0.01$) causes a rapid, decadal scale outward migration of the outer annulus; (ii) the resonances on the inner annulus are weaker, but t_{mig} remains geologically short (\lesssim Myr) for $A-B \gtrsim 5$ km; (iii) even ~ 5 -km topographic features are sufficient to induce migration time scales of a few Myr.

Numerical simulations can test those mechanisms. Global collisional codes have been run²², but with no torque appearing as the potentials considered were axisymmetric. Other local simulations do consider elongated bodies²³, but not rotating, hampering again any torque. Here we performed numerical integrations using a simple Stokes-like friction acting on the particles,

$$\gamma_{\text{Stokes}} = -\eta\Omega\mathbf{v}_r, \quad (5)$$

where \mathbf{v}_r is the particle radial velocity and η is a dimensionless friction coefficient. This friction dissipates energy while conserving angular momentum, thus being a good proxy for collisions at low computing cost. Fig. 3 shows results using $\eta = 0.01$ (see Methods for the choice of η). As mentioned earlier, the specific form of γ_{Stokes} and the value of η have little effects on the resonant torque Γ_m , when compared to more realistic situations including collisions and self-gravity.

We have checked numerically the dependence $t_{\text{mig}} \propto \mathcal{A}_m^{-2}$ (Eq. (4)). This permits to save computing time in the case of a mass anomaly by using $\mu = 0.005$ (instead of $\sim 10^{-5}$), hence speeding up migration time scales by a factor $500^2 = 2.5 \times 10^5$, an effect accounted for in Fig. 3a,b,c,d. In contrast, the integration shown in Fig. 3e,f,g,h uses a realistic Chariklo's elongation $\epsilon = 0.20$, with no further corrections applied. Fig. 3 confirms our calculations, i.e. (i) the rapid infall of particles onto Chariklo's equator inside the corotation radius, exacerbated by the fact that the large orbital eccentricities enhance collisions with the body, and due to the unstable character of the C_2 and C_4 points for $\epsilon = 0.20$ (Fig. 1); (ii) the strong torques up to the 1/2 resonance, that pushes the disk material outwards. Our integrations actually show that inward of the 1/2 resonance, and between discrete LR, the orbital eccentricities remain sufficiently excited to cause a slower but still significant migration away from the corotation radius.

A LR opens a cavity in the disk if Γ_m exceeds the viscous torque¹⁹ $\Gamma_\nu = 3\pi na^2\nu\Sigma_0$, where the kinematic viscosity $\nu = h^2n$ is related to the ring vertical thickness h , see Methods. From Eq. (3), we obtain

$$\left| \frac{\Gamma_m}{\Gamma_\nu} \right| \sim \frac{4\pi}{9q^{4/3}} \left(\frac{m-1}{m} \right)^{5/3} \left(\frac{R}{h} \right)^2 \mathcal{A}_m^2. \quad (6)$$

Using $h \sim 10$ m (see Methods) and $z \sim 5$ km we get $|\Gamma_{-2}/\Gamma_\nu| \sim 3 \times 10^{-2}$ for $m = -2$ (2/3 outer LR). Thus, a 5-km feature is too weak to open a cavity, but not by much owing to the steep dependence of $\mathcal{A}_m^2 \propto \mu^2 \propto z^6$. In contrast, the torque exerted by an ellipsoid with $\epsilon = 0.20$ is overwhelming (by six orders of magnitude) at the 2/3 LR compared to Γ_ν . Since $\mathcal{A}_{-2} \propto \epsilon$ (see Methods), ellipsoids with $A-B$ as small as 0.1 km are actually able to carve a cavity inside the 2/3 LR.

Chariklo and Haumea's elongations considered here are large enough to strongly perturb a ring near the 1/2 resonance, although no torque formula is available at that resonance in the ellipsoid case, because it is of second order nature (it must actually be noted 2/4, and is not a LR, see Methods). This said, the final radius of the cavity depends on processes that are not considered here, since our friction law is an oversimplification of actual collisions. More importantly, accretion into satellites takes over as the Roche limit is approached, leading to

complex ring-satellites interaction like shepherding. Nevertheless, our results show that either due to mass anomalies or body elongation, rings should not exist inward of the 1/2 resonance at $a_{1/2} = 2^{2/3}a_{\text{cor}}$. This is consistent with what is observed for Chariklo and Haumea.

In fact, the ring existence requires that a space exists between $a_{1/2}$ and the Roche limit a_{Roche} , to prevent the ring accretion into satellites. From $a_{\text{Roche}} \sim (3/\gamma)^{1/3}(M/\rho')^{1/3}$, where ρ' is the density of the ring particles, and γ is a factor describing the particle shape²⁴, the condition $a_{1/2} < a_{\text{Roche}}$ reads

$$\gamma\rho' \lesssim \frac{3\Omega^2}{4G}. \quad (7)$$

Thus, a non-axisymmetric body must rotate fast enough and/or the particles be underdense enough for a ring to exist. Although γ and ρ' are poorly known, we can consider the preferred value $\gamma = 1.6$ that describes particles filling their lemon-shaped Roche lobes²⁵, and $\rho' \sim 450 \text{ kg m}^{-3}$, typical of the small moons orbiting near Saturn's rings²⁶, and a good proxy of ring particle densities. Eq. (7) then requires rotation periods shorter than about 7 h, a condition met by both Chariklo and Haumea.

Our model predicts that the inner part of the disk may be deposited on the equator of the body, forming a ridge akin to that of the Saturnian satellite Iapetus. It has been proposed that this ridge is due to the presence of a transient ring that rained down onto Iapetus' equator due to the torque from of a former subsatellite^{27–29}. This may happen on short time scales. For instance Eq. (4) shows that a 10 km-radius satellite orbiting at 500 km pushes an initial disk extending from the surface to 400 km in less than 1 Myr. In our case, the disk decay is caused by the body itself. The infall time scales being of many years (Fig. 2), impact angles on the surface are very shallow, with velocities less than a km s^{-1} , ensuring that the material piles up as a ridge instead of forming craters. Future stellar occultations might detect such ridges on Chariklo or Haumea.

In a broader and more speculative perspective, it is interesting to consider the orbital distribution of satellites of asteroids and Trans-Neptunian Objects. Supplementary Fig. 1 displays the histogram of the satellite orbital periods, expressed in units of the rotation periods of the primaries. Apart from a conspicuous peak corresponding to synchronous, tidally evolved orbits, this histogram indicates a clearing between the corotation radius and the outer 1/2 resonance, followed by a steady increase beyond this resonance. This distribution might be the signature of satellite formation proceeding from an initial collisional disk that has been pushed away by the resonant mechanism described here.

References

1. Braga-Ribas, F. *et al.* A ring system detected around the Centaur (10199) Chariklo. *Nature* **508**, 72–75 (2014).
2. Ortiz, J.L. *et al.* The size, shape, density and ring of the dwarf planet Haumea from a stellar occultation. *Nature* **550**, 219–223 (2017).
3. Ortiz, J.L. *et al.* Possible ring material around centaur (2060) Chiron. *Astron. Astrophys.* **576**, A18 (2015).
4. Ruprecht, J.D. *et al.* 29 November 2011 stellar occultation by 2060 Chiron: Symmetric jet-like features. *Icarus* **252**, 271–276 (2015).
5. Esposito, L.W. Planetary rings. *Rep. Prog. Phys.* **65**, 1741–1783 (2002).

6. Sicardy, B., El Moutamid, M., Quillen, A.C., Schenk, P., Showalter, M.R. & Walsh, K. in *Planetary ring systems* (eds Tiscareno, M. S. & Murray, C.D.) 135153 (Cambridge Univ. Press, 2018).
7. Pan, M. & Wu, Y. On the mass and origin of Chariklo's rings. *Astrophys. J.* **821**, 18 (2016).
8. Hyodo, R., Charnoz, S., Genda, H. & Ohtsuki, K. Formation of centaurs' rings through their partial tidal disruption during planetary encounters. *Astrophys. J. Lett.* **828**, L8 (2016).
9. Araujo, R.A.N., Sfair, R. & Winter, O.C. The rings of Chariklo under close encounters with the giant planets. *Astrophys. J.* **824**, 80 (2016).
10. Wood, J., Horner, J., Hinse, T.C. & Marsden, S.C. The Dynamical History of Chariklo and Its Rings. *Astron. J.* **153**, 245 (2017).
11. Melita, M.D., Duffard, R., Ortiz, J.L. & Campo-Bagatin, A. Assessment of different formation scenarios for the ring system of (10199) Chariklo. *Astron. Astrophys.* **602**, A27 (2017).
12. Leiva, R. *et al.* Size and Shape of Chariklo from Multi-epoch Stellar Occultations. *Astron. J.* **154**, 159 (2017).
13. Hedman, M.M. & Nicholson, P.D. More Kronoseismology with Saturn's rings. *Mon. Not. R. Astron. Soc.* **444**, 1369–1388 (2014).
14. Morais, M.H.M. & Giuppone, C.A. Stability of prograde and retrograde planets in circular binary systems. *Mon. Not. R. Astron. Soc.* **424**, 52–64 (2012).
15. Goldreich, P. & Tremaine, S. The excitation of density waves at the Lindblad and corotation resonances by an external potential. *Astrophys. J.* **233**, 857–871 (1979).
16. Hopkins, P.F. & Quataert, E. An analytic model of angular momentum transport by gravitational torques: from galaxies to massive black holes. *Mon. Not. R. Astron. Soc.* **415**, 1027–1050 (2011).
17. Lin, D.N.C. & Papaloizou, J. Tidal torques on accretion discs in binary systems with extreme mass ratios. *Mon. Not. R. Astron. Soc.* **186**, 799–812 (1979).
18. Goldreich, P. & Tremaine, S. Disk-satellite interactions. *Astrophys. J.* **241**, 425–441 (1980).
19. Goldreich, P. & Tremaine, S. The dynamics of planetary rings. *Ann. Rev. Astron. Astro.* **20**, 249–283 (1982).
20. Meyer-Vernet, N. & Sicardy, B. On the physics of resonant disk-satellite interaction. *Icarus* **69**, 157–175 (1987).
21. Marley, M.S. & Porco, C.C. Planetary acoustic mode seismology: Saturn's rings *Icarus* **106**, 508–524 (1993).
22. Michikoshi, S. & Kokubo, E. Simulating the Smallest Ring World of Chariklo. *Astrophys. J. Letters* **837**, L13 (2017).
23. Gupta, A., Nadkarni-Ghosh, S. & Sharma, I. Rings of non-spherical, axisymmetric bodies. *Icarus* **199**, 97–116 (2018).
24. Tiscareno, M.S., Hedman, M.M., Burns, J.A. & Castillo-Rogez, J. Compositions and Origins of Outer Planet Systems: Insights from the Roche Critical Density. *Astrophys. J. Lett.* **765**, L28 (2013).
25. Porco, C.C., Thomas, P.C., Weiss, J.W. & Richardson, D.C. Saturn's small inner satellites: clues to their origins. *Science* **318**, 1602 (2007).

26. Thomas, P.C. Sizes, shapes, and derived properties of the saturnian satellites after the Cassini nominal mission. *Icarus* **208**, 395–401 (2010).
27. Ip, W.-H. On a ring origin of the equatorial ridge of Iapetus *Geophys. Res. Lett.* **33**, L16203 (2006).
28. Levison, H.F., Walsh, K.J., Barr, A.C. & Dones, L. Ridge formation and de-spinning of Iapetus via an impact-generated satellite. *Icarus* **214**, 773–778 (2011).
29. Dombard, A.J., Cheng, A.F., McKinnon, W.B. & Kay, J.P. Delayed formation of the equatorial ridge on Iapetus from a subsatellite created in a giant impact. *J. Geophys. Res.* **117**, E03002 (2012).
30. Fornasier, S. *et al.* The Centaur 10199 Chariklo: investigation into rotational period, absolute magnitude, and cometary activity. *Astron. Astrophys.* **568**, L11 (2014).
31. Lellouch, E. *et al.* “TNOs are cool”: a survey of the trans-Neptunian region. II. The thermal lightcurve of (136108) Haumea. *Astron. Astrophys.* **518**, L147 (2010).
32. Ragozzine, D. & Brown, M.E. Orbits and masses of the satellites of the dwarf planet Haumea (2003 EL₆₁). *Astron. J.* **137**, 4766–4776 (2009).
33. Balmino, G. Gravitational potential harmonics from the shape of an homogeneous body. *Celest. Mech. Dyn. Astr.* **60**, 331–364 (1994).
34. Boyce, W. Comment on a Formula for the Gravitational Harmonic Coefficients of a Triaxial Ellipsoid. *Celestial Mechanics and Dynamical Astronomy* **67**, 107–110 (1997).
35. Dermott, S.F. & Murray, C.D. The dynamics of tadpole and horseshoe orbits. I. Theory. *Icarus* **48**, 1–11 (1981).
36. Schmidt, J. *et al.* Dynamics of Saturn’s dense rings. in Saturn from Cassini-Huygens (eds Dougherty, M.K., Esposito, L.W. & Krimigis S.M.) 413–458 (Springer, 2009).
37. Murray, C.D. & Dermott, S.F. Solar system dynamics Cambridge University Press (1999).

Acknowledgements

The work leading to this results has received funding from the European Research Council under the European Community’s H2020 2014-2020 ERC Grant Agreement No. 669416 “Lucky Star”. P.S.S. acknowledges financial support by the European Union’s Horizon 2020 Research and Innovation Programme, under Grant Agreement No. 687378. We thank Françoise Combes for discussions on corotation and Lindblad resonances in the context of galactic dynamics, and Timothée Vaillant for comments on satellite formations and migrations. We thank the reviewers for comments that improved the content and presentation of this work.

Author contributions

B.S., R.L. and M.E.M. contributed to the analytical calculations that describe the resonance dynamics around a non-axisymmetric body. B.S. wrote the paper and made the figures, with contributions from R.L., S.R., F.R. and P.S.S. F.R. provided insights for the application of this work to the formation of satellites around small bodies. Numerical integrations were independently performed by B.S, S.R. and F.R.

Competing interests

The authors declare no competing interests.

Author information Correspondence and requests for materials should be addressed to B.S. at bruno.sicardy@obspm.fr.

Author Data and code availability The data that support the plots within this paper and other findings of this study are available from the corresponding author upon reasonable request. We have opted not to make our codes available as we cannot guarantee their correct performance on different computing platforms.

Table 1 - Chariklo and Haumea's adopted parameters^(a)

Parameters	Chariklo	Haumea
Rotation period, T_{rot} (h) (refs. 30, 31)	7.004	3.915341
Mass M (kg) (refs. 12, 32)	6.3×10^{18}	4.006×10^{21}
Rotational parameter $q^{(b)}$	0.226	0.268
Semi-axes $A \times B \times C$ (km) (refs. 2, 12)	$157 \times 139 \times 86$	$1161 \times 852 \times 513$
Reference radius $R^{(c)}$ (km)	115	712
Elongation parameter ^(d) $\epsilon = (A^2 - B^2)/2R^2$	0.20	0.61
Oblateness parameter ^(d) $f = (A^2 + B^2 - 2C^2)/4R^2$	0.55	0.76
Height of topographic feature $z^{(e)}$ (km)	5	n.a.
Corotation radius $a_{\text{cor}}^{(f)}$ (km)	189	1104
Outer 1/2 (or 2/4) resonance radius $a_{1/2}^{(g)}$ (km)	300	1752
Classical Roche limit $a_{\text{Roche}}^{(h)}$ (km)	280	2400
Ring radii (km) (refs. 1, 2)	390 and 405	2287

^(a) No error bars are considered here, the adopted parameters being representative of typical cases examined in this work.

^(b) See Eq. (1).

^(c) Defined as $R = \sqrt{3}(1/A^2 + 1/B^2 + 1/C^2)^{-1/2}$, see Methods Eq. (16).

^(d) See Methods Eq. (18).

^(e) Assuming a spherical body of radius $R_{\text{sph}} = 129$ km (ref. 12). This corresponds to a mass anomaly $\mu \sim (z/2R_{\text{sph}})^3 \sim 10^{-5}$.

^(f) Using $a_{\text{cor}} = Rq^{-1/3}$, from Eq. (1) and Kepler's third law.

^(g) Using $a_{1/2} = 2^{2/3}a_{\text{cor}}$, from Kepler's third law.

^(h) Using the classical expression $a_{\text{Roche}} \sim (3/\gamma)^{1/3}(M/\rho')$, with $\gamma = 0.85$ and icy ring particles with density $\rho' = 1000$ kg m⁻³. More realistic values of γ and ρ' are discussed in the text.

Figure legends

Figure 1 | Corotation and Lindblad resonances around Chariklo. In both panels (topographic feature on the left, elongated body on the right), the red (resp. blue) circles correspond to inner (resp. outer) $m/(m-1)$ Lindblad resonance (LR) radii with $m > 1$ (resp. $m < 0$), see Eq. (2). The black lines show isopotential curves in a frame corotating with Chariklo, and the gray lines outline the limb of the body. The dots C_1, \dots, C_4 mark the corotation fixed points. The points C_2 and C_4 are local potential maxima and are linearly stable if the mass anomaly or the elongation of the body are not too large, see Methods. Left - A topographic feature of height $z = 5$ km (gray half dome, not on scale) is sitting at the surface a body of radius $R_{\text{sph}} = 129$ km, and corresponds to a mass anomaly $\mu \sim 10^{-5}$. For better viewing, the isopotential black lines have been radially stretched by a factor of 50 with respect to the corotation radius. A few inner ($m = 2, 3, 4, 5$) and outer ($m = -1, -2, -3, -4$) LR radii are shown. Right - The same for a Chariklo shape solution with elongation $\epsilon = 0.20$. The limb of the body and the isopotential lines are plotted on scale. Only LRs with m even are now allowed, the inner one corresponding to $m = 6$, and the two outer ones corresponding to $m = -2, -4$. The green curve is an orbit that starts at C_2 without applying any friction (conservative case). It is unstable because the elongation ϵ is larger than the critical value $\epsilon_{\text{crit}} = 0.16$ (see Methods), leading to a collision with the body after three months in the example shown here.

Figure 2 | Torques strengths at Lindblad Resonances around Chariklo and migration time scales. **a**, The dimensionless coefficients \mathcal{A}_m^2 providing the torque value at $m/(m-1)$ Lindblad resonances (Eq. (3)) vs. the resonant radii on each side of the corotation radius (dotted line). The values of \mathcal{A}_m are evaluated from Supplementary Table 1, using a Chariklo equatorial topographic feature of height $z = 5$ km, corresponding to a mass anomaly $\mu = 10^{-5}$ (blue squares), or a difference of semi-axes $A - B = 18$ km (Table 1), corresponding to an elongation parameter $\epsilon = 0.20$ (red squares). Note the steep decrease of the torques as the corotation radius is approached, due to the exponential decrease of \mathcal{A}_m^2 as $|m|$ increases, see Methods. The light gray region at left encloses Chariklo's largest semi-axis $A = 157$ km, inside which particles collide with the body in the ellipsoidal case, while the dark gray region encloses Chariklo's radius $R_{\text{sph}} = 129$ km in the spherical case (Table 1). **b**, Solid lines: migration times (Eq. (4)) of an outer annulus of width 100 km that extends outside the corotation (see **a**), either due to the topographic features (blue) of heights z or ellipsoids with various $A - B$ (red). Dotted lines: the same for an inner annulus of width 20 km in the ellipsoidal case, and 60 km in the spherical case, see **a**.

Figure 3 | Migration of ring particles around Chariklo. The particles are submitted to Chariklo's gravitational field (topographic feature on the left, elongated body on the right), plus a radial Stokes-like friction with $\eta = 0.01$ (Eq. (5)). The radii of the corotation point C_2 (a_{cor}), the 2/3 and 1/2 outer Lindblad Resonances (LRs) between the particle mean motions and Chariklo's rotation period are marked at the bottom, together with the location of Chariklo's main ring¹ C1R. **a, b, c, d**, The effect of an equatorial topographic feature (black dot) with mass $\mu = 5 \times 10^{-3}$ relative to Chariklo. Initially, 701 particles are regularly placed between $0.7a_{\text{cor}}$ and $2.2a_{\text{cor}}$. In all panels, each particle is plotted over twenty regular time steps spanning 40,000 years. **a**, After 40,000 years, the clearing of the corotation region is ongoing; **b**, After 2.5×10^5 years, some particles remain near C_2 , while others are pushed outside the 2/3 LR; **c**, After 2.5×10^6 years, all the particles inside the corotation radius and near C_2 have collided with Chariklo; **d**, After 6.3×10^6 years, all the remaining particles are now outside the 1/2 LR. **e**,

f, g, h, Effect of an ellipsoid with elongation $\epsilon = 0.20$, displayed with its longest axis face on. The particles now start between $1.1a_{cor}$ and $2.2a_{cor}$ (particles inside $1.1a_{cor}$ collide with Chariklo after a few days). **e**, After three months, most of the particles have been pushed outside the 2/3 LR; **f, g** and **h**, After one, five and twelve years, respectively, all the particles have either collapsed onto Chariklo, or continue their outward migration at decreasing pace outside of the 2/4 resonance. Note that time scales of same order (but shorter) would be obtained for particles orbiting around Haumea, which has a larger elongation $\epsilon = 0.61$.

Supplementary Figure 1 | Distribution of orbital periods of satellites around asteroids and Trans-Neptunians Objects. The orbital period P_s of 179 satellites known around binary or multiple asteroids and Trans-Neptunians Objects (taken from <http://www.johnstonsarchive.net/astro/astmoontable.html> as of April 2018) are plotted in units of the rotation period P_p of their primaries. The resulting histogram of P_s/P_p shows a peak near unity, corresponding to tidally evolved systems, in which the primary rotates synchronously with the satellite orbital period. The vertical dotted line correspond to the outer 1/2 resonance, where the satellite completes one revolution while the primary completes two rotations. The steady increase of satellite presence beyond that resonance is in line with the model presented in the text, i.e. satellite formation in a primordial collisional disk that has been pushed outwards by the resonant torque of the 1/2 resonance.

Supplementary Figure 2 | Phase portrait of the 2/4 outer spin-orbit resonance. The phase portrait of the 2/4 resonance is shown for an ellipsoidal Chariklo with elongation $\epsilon = 0.20$ (Table 1), with $X = e \cos(\phi_{2/4})$ and $Y = e \sin(\phi_{2/4})$, where e is the particle eccentricity, $\phi_{2/4} = 2\lambda - \lambda_A - \varpi$ is the resonant angle, and the various other angles are defined in the Methods. All the trajectories share the same Jacobi constant, see Murray & Dermott, Solar system dynamics, Cambridge University Press (1999) for details. This constant has been chosen so that the particle that starts at the origin $(X, Y) = (0, 0)$ is at exact resonance, i.e. with semi-major axis $a_{2/4} = a_{1/2}$, see Main Text. The origin is then an unstable hyperbolic point that forces particles initially on a circular orbit to acquire high eccentricities of the order of $e \sim 0.2$, see Methods. This kind of topology occurs for a narrow semi-major axis range of $a_{1/2}(1 - 0.25\epsilon) \lesssim a \lesssim a_{1/2}(1 + 0.25\epsilon)$ around the resonance.

Methods

We calculate the potential outside a body in two simple cases: a topographic feature located at the equator of a spherical object and a homogeneous triaxial ellipsoid. Calculations are restricted to the equatorial plane of the body, where a collisional disk is expected to settle.

Topographic feature

We consider a spherical body of mass M , radius R_{sph} and center \mathcal{C} with an equatorial topographic feature of mass μ relative to the mass of the body, that rotates with period T_{rot} and angular velocity $\Omega = 2\pi/T_{\text{rot}}$. We denote O the center of mass of the body plus the topographic feature, \mathbf{r} the position vector of the particle, measured from the center of the body, $r = \|\mathbf{r}\|$, $\theta = L - L_A$, where L is the true longitude of the particle, and $L_A = \Omega t$ is the orientation angle of the topographic feature, counted from an arbitrary origin. Finally, \mathbf{R} is the vector that connects the center of mass O to the topographic feature and $\Delta = \mathbf{r} - \mathbf{R}$. The potential acting on the particle at position \mathbf{r} in a frame fixed at \mathcal{C} is:

$$U(\mathbf{r}) = -\frac{GM}{r} - \mu \frac{GM}{\Delta} + \Omega^2 (\mathcal{C}\mathbf{O} \cdot \mathbf{r}), \quad (8)$$

where the last term is the indirect part stemming from the motion of \mathcal{C} around O . Using $\mathcal{C}\mathbf{O} = \mu\mathbf{R}$ and the definition of the rotational parameter q (Main Text Eq. (1)), we obtain

$$U(\mathbf{r}) = -\frac{GM}{r} - GM\mu \left[\frac{1}{\Delta} - q \frac{\mathbf{R} \cdot \mathbf{r}}{R_{\text{sph}}^3} \right] = \quad (9)$$

$$-\frac{GM}{r} - \frac{GM}{2R_{\text{sph}}} \mu \left\{ \left[\sum_{m=-\infty}^{+\infty} b_{1/2}^{(m)}(r/R_{\text{sph}}) \cos(m\theta) \right] - 2q \left(\frac{r}{R_{\text{sph}}} \right) \cos(\theta) \right\},$$

where the $b_{1/2}^{(m)}$'s are the classical Laplace coefficients.

Homogeneous triaxial ellipsoid

We now consider a homogeneous triaxial ellipsoid of mass M and semi-axes $A > B > C$. The potential $U(\mathbf{r})$ can again be expanded in a series in $\cos(m\theta)$, where θ is now the difference between the true longitude of the particle and the orientation of the largest axis of the ellipsoid. Only even values of m must appear to ensure the invariance of the potential under a rotation of π radians. Thus, posing $m = 2p$,

$$U(\mathbf{r}) = \sum_{p=-\infty}^{+\infty} U_{2p}(r) \cdot \cos(2p\theta). \quad (10)$$

In the 3-D case, we use the Eq. (64) of ref. 33, where the m index used by this author is replaced by p in our version. Correcting for the typo of ref. 33, in which the index m should vary from 0 to l (and not from 1 to l):

$$U(\mathbf{r}) = -\frac{GM}{r} \left\{ \sum_{p=0}^{+\infty} \cos(2p\theta) \left[\sum_{l=p}^{+\infty} \left(\frac{R}{r} \right)^{2l} C_{2l,2p} P_{2l,2p}(\sin \varphi) \right] \right\}, \quad (11)$$

where φ is the latitude. The coefficient $P_{l,p}$ is the associated Legendre polynomial, whose classical expression is

$$P_{l,p}(u) = (-1)^p \frac{(1-u^2)^{p/2}}{2^l l!} \frac{d^{l+p}}{du^{l+p}} [(u^2-1)^l]. \quad (12)$$

Note that the factor $(-1)^p$ is absent in Eq. (2) of ref. 33, but is transferred to the coefficient K_{lp} used by this author (his Eq. (3)).

Here we consider particles moving in the equatorial plane of the body, i.e. $\varphi = 0$. Using the binomial expansion of $(u^2 - 1)^l$, we obtain:

$$P_{2l,2p}(0) = (-1)^{(l-p)} \frac{(2l+2p)!}{2^{2l}(l+p)!(l-p)!} \quad (13)$$

Moreover, from the last equation of ref. 34, we have:

$$C_{2l,2p} = \frac{3}{R^{2l}} \frac{l!(2l-2p)!}{2^{2p}(2l+3)(2l+1)!} \left(2 - \delta_{(0,p)}\right) \times \sum_{i=0}^{\text{int}(\frac{l-p}{2})} \frac{(A^2 - B^2)^{p+2i} \left[C^2 - \frac{1}{2}(A^2 + B^2)\right]^{l-p-2i}}{16^i (l-p-2i)!(p+i)!i!}, \quad (14)$$

where $\delta_{(0,p)}$ is the Kronecker delta function. Because we want both negative and positive values of p in Eq. (10), it is convenient to modify Eq. (11) so that p varies from $-\infty$ and $+\infty$. This can be accommodated by replacing the factor $(2 - \delta_{(0,p)})$ by 1 in Eqs. 14, and replacing p by $|p|$ when calculating $P_{2l,2p}$ and $C_{2l,2p}$. Thus,

$$U_{2p}(r) = -\frac{GM}{r} \sum_{l=|p|}^{+\infty} \left(\frac{R}{r}\right)^{2l} Q_{2l,2|p|}, \quad (15)$$

where $Q_{2l,2|p|} = C_{2l,2|p|} P_{2l,2|p|}(0)$. Moreover, the reference radius R is defined by

$$\frac{3}{R^2} = \frac{1}{A^2} + \frac{1}{B^2} + \frac{1}{C^2}. \quad (16)$$

Finally, a closed form of $U(\mathbf{r})$ outside the body that depends on A , B and C can be derived, with

$$Q_{2l,2|p|} = \frac{3}{2^{l+2|p|}(2l+3)} \frac{(2l+2|p|)!(2l-2|p|)!l!}{(l+|p|)!(l-|p|)!(2l+1)!} \times \sum_{i=0}^{\text{int}(\frac{l-|p|}{2})} \frac{1}{16^i} \frac{\epsilon^{|p|+2i}}{(|p|+i)!i!} \frac{f^{l-|p|-2i}}{(l-|p|-2i)!}. \quad (17)$$

The dimensionless parameters ϵ and f measure the elongation and oblateness of the body, respectively:

$$\epsilon = \frac{A^2 - B^2}{2R^2} \quad \text{and} \quad f = \frac{A^2 + B^2 - 2C^2}{4R^2}. \quad (18)$$

Note that in the limiting case where ϵ tends to zero, $\epsilon \sim (A - B)/A$. In the limiting case where f tends to zero and the body is axisymmetric ($\epsilon = 0$), $f \sim (A - C)/A$, the usual definition of oblateness.

The term $Q_{2l,2|p|}$ is of order l in (ϵf) . For evaluating the effect of Lindblad resonances, it is enough to consider the term of lowest order in R/r in Eq. (15), corresponding to $l = |p|$. Defining the sequence $S_{|p|} = Q_{2|p|,2|p|}/\epsilon^{|p|}$ and from $m = 2p$, we obtain

$$U(\mathbf{r}) = -\frac{GM}{r} \sum_{m=-\infty}^{+\infty} \left(\frac{R}{r}\right)^{|m|} S_{|m/2|} \epsilon^{|m/2|} \cos(m\theta) \quad (m \text{ even}), \quad (19)$$

where $S_{|p|}$ is recursively given by

$$S_{|p|+1} = 2 \frac{(|p| + 1/4)(|p| + 3/4)}{(|p| + 1)(|p| + 5/2)} \times S_{|p|} \quad \text{with} \quad S_0 = 1. \quad (20)$$

The potential (19) has been implemented in numerical schemes to integrate the motion of particles around an elongated body (adding the Stokes-like friction of Main Text Eq. (5)). We have truncated the expansion of the potential above $|m| > 10$, which is justified by the fact that the resonance strength rapidly decreases as m increases (Fig. 2). In the numerical integrations, the initial velocities assigned to the particles is simply the local circular keplerian velocity around a body of mass M . The Stokes-like friction rapidly damps any radial motions caused by this choice, over a transient time scale $1/\eta\Omega$. Taking $\eta = 0.01$ (see below), this corresponds to about 15 revolutions around the body, a short time compared to the integrations performed here.

Moreover, Eq. (15) yields the axisymmetric part of the potential by making $p = 0$,

$$U_0(r) = -\frac{GM}{r} \sum_{l=0}^{+\infty} Q_{2l,0} \left(\frac{R}{r}\right)^{2l}, \quad (21)$$

which in turns provides the particle mean motion and horizontal epicyclic frequency:

$$n^2(r) = \frac{1}{r} \frac{dU_0(r)}{dr} \quad \text{and} \quad \kappa^2(r) = \frac{1}{r^3} \frac{d(r^4 n^2)}{dr}. \quad (22)$$

In our numerical integrations, we have kept the lowest order term in R/r , corresponding to $l = 1$, i.e. $U_0(r) = -(GM/r) [1 + (f/5)(R/r)^2]$. Identification with classical formulae shows that this corresponds to a body with dynamical oblateness $J_2 = (2/5)f$. This approximation provides:

$$n^2(r) \sim \frac{GM}{r^3} \left[1 + \frac{3f}{5} \left(\frac{R}{r}\right)^2 \right] \quad \text{and} \quad \kappa^2(r) \sim \frac{GM}{r^3} \left[1 - \frac{3f}{5} \left(\frac{R}{r}\right)^2 \right] \quad (23)$$

Expansion of the disturbing function

The potential in Eq. (9) can be expressed as $U(\mathbf{r}) = -GM/r - \mathcal{R}$, where \mathcal{R} is the classical disturbing function:

$$\mathcal{R}(\mathbf{r}) = \frac{GM}{2R_{\text{sph}}} \mu \left\{ \left[\sum_{m=-\infty}^{+\infty} b_{1/2}^{(m)}(r/R_{\text{sph}}) \cos(m\theta) \right] - 2q \left(\frac{r}{R_{\text{sph}}}\right) \cos(\theta) \right\} \quad (24)$$

It can be expressed in terms of the orbital elements of the particle, a , e , λ and ϖ (semi-major axis, eccentricity, mean longitude and longitude of periape, respectively), using e.g. the formalism presented in Chapter 6 and Appendix B of ref. 37 to describe perturbations by a satellite. This transformation uses operators f_n that contain multiplications by powers of the ratio $\beta = a/R_{\text{sph}}$ and the differential operator $D = d/d\beta$. The only difference with the case of satellite perturbations is that the ratio a/R_{sph} replaces the ratio a/a_s , where a_s is the satellite semi-major axis.

In the case of an ellipsoid, \mathcal{R} is derived from Eq. (19),

$$\mathcal{R}(\mathbf{r}) = \frac{GM}{r} \sum_{m=-\infty(m \neq 0)}^{+\infty} \left(\frac{R}{r}\right)^{|m|} S_{|m/2|} \epsilon^{|m/2|} \cos(m\theta) \quad (25)$$

The same formalism as in ref. 37 can be applied, i.e. using exactly the same operators f_n . Identifications term by term in the summations above show that it is sufficient for that to replace R_{sph} by R and $\mu b_{1/2}^{(m)}(r/R_{\text{sph}})$ by $2(R/r)^{|m|+1} S_{|m/2|} \epsilon^{|m/2|}$.

Corotation resonance

The potential near the corotation radius a_{cor} , as observed in a frame corotation with the body, is

$$V(\mathbf{r}) = U(\mathbf{r}) - \frac{\Omega^2 r^2}{2} \sim -\frac{3}{2}\Omega^2 a_{\text{cor}}^2 \left(\frac{\Delta r}{a_{\text{cor}}}\right)^2 - \frac{GM}{a_{\text{cor}}} f(\theta) = -\frac{3}{2}\Omega^2 a_{\text{cor}}^2 \left(\frac{\Delta r}{a_{\text{cor}}}\right)^2 - \frac{\Omega^2 R^2}{q^{2/3}} f(\theta), \quad (26)$$

where the azimuthal function $f(\theta)$ is given in Supplementary Table 1, and $\Delta r = r - a_{\text{cor}} \ll a_{\text{cor}}$. Examples of isopotential levels for the two cases examined here are displayed in Fig. 1. Note that the corotation points associated with the mass anomaly mimic the Lagrange points L_1, \dots, L_5 , except that L_1 and L_2 have merged into a single saddle point C_1 where the potential remains finite. Also, the points C_2 and C_4 are close to but not at 60 degrees from C_1 . That angle actually depends on q (see Supplementary Table 1) and is close to 70 deg in the particular example displayed in Fig. 1.

Near a_{cor} , the particles follow the trajectory $(3/8)(\Delta r/a_{\text{cor}})^2 + f(\theta) \sim \text{constant}$. They are nothing else than the level curves of the potential in a frame corotating with the body (Fig. 1), except for a dilation by a factor two with respect to a_{cor} (ref. 35). The full radial width of the trajectory is then $W_{\text{cor}} = 2\sqrt{8\Delta f/3}$, where $\Delta f = f_{\text{max}} - f_{\text{min}}$ is the total variation of $f(\theta)$ over $[0, 2\pi[$.

For order of magnitude considerations, we note that $\Delta f \sim \mu$ for the case of the mass anomaly. In the case of the ellipsoid, and for sake of estimation, we can simplify the expression (19) further by taking the lowest orders $p = 0$ and $|p| = 1$, i.e. (noting that $S_1 = 0.15$)

$$V(\mathbf{r}) \sim -\frac{3}{2}\Omega^2 a_{\text{cor}}^2 \left(\frac{\Delta r}{a_{\text{cor}}}\right)^2 - \frac{3}{10}R^2\Omega^2\epsilon \cos(2\theta), \quad (27)$$

so that $f(\theta) \sim (3/10)q^{2/3}\epsilon \cos(2\theta)$ and thus $\Delta f \sim (3/5)q^{2/3}\epsilon$, from which we derive

$$W_{\text{cor},\mu} \sim 4Rq^{-1/3}\sqrt{\frac{2}{3}\mu} \quad \text{and} \quad W_{\text{cor},\epsilon} \sim 4R\sqrt{\frac{2}{5}\epsilon}. \quad (28)$$

in each of the two cases examined here. For a typical Chariklo topographic feature ($\mu \sim 10^{-5}$), we obtain a narrow corotation region with $W_{\text{cor},\mu} \sim 2$ km only, while for $\epsilon \sim 0.20$, $W_{\text{cor},\epsilon} \sim 130$ km, meaning that the corotation region fills in all the space between a_{cor} and Chariklo's surface (Fig. 1).

If ring arcs are present near C_2 and C_4 , they should be destroyed by viscous spreading time scales $t_{\text{spread}} \sim W_{\text{cor}}^2/\nu$, where ν is the kinematic viscosity. This quantity can be parametrized as $\nu = h^2 n$, where h typically represents, for a dense disk, the size of the largest particles, or equivalently, the vertical thickness of the ring³⁶. The local velocity field in Chariklo or Haumea's rings are comparable to those of Saturn¹. Consequently, the collisional physics in those systems is expected to be similar⁶, i.e. $h \sim 10$ meters (ref. 36). From the expressions of W_{cor} derived above, we obtain $t_{\text{spread},\mu} \sim 2\mu(R/h)^2 T_{\text{rot}}$ for a mass anomaly μ , and $t_{\text{spread},\epsilon} \sim \epsilon(R/h)^2 T_{\text{rot}}$ for an ellipsoid. With $\mu \sim 10^{-5}$, we obtain very short escape times (a few years) of the arc material from the corotation region, if caused by a mass anomaly. The spreading time is longer, some 10^4 years, but still geologically short if the corotation is controlled by an ellipsoid with elongation $\epsilon \sim 0.20$.

The corotation points C_2 and C_4 are linearly unstable if the potential $V(\mathbf{r})$ meets the condition

$$(4\Omega^2 + V_{xx} + V_{yy})^2 \leq V_{xx}V_{yy} - V_{xy}^2, \quad (29)$$

where the indices x and y are short-hand notations for partial derivatives³⁷.

For the classical L_4 and L_5 points (corresponding to $q = 1$), this condition leads to the Gascheau-Routh criterium $\mu > 0.0385\dots$. For the cases examined here, q is smaller than but of order unity, so that the critical value of μ remains close to 0.04. This value is safely avoided for Chariklo, as it would correspond to an unrealistic feature with $z = 80$ km.

In the case of the ellipsoid, it is found from Eqs. (27) and (29) that C_2 and C_4 are unstable for:

$$\epsilon > \epsilon_{\text{crit}} \sim \frac{0.06}{q^{2/3}}. \quad (30)$$

Using $q = 0.226$ for Chariklo implies $\epsilon_{\text{crit}} \sim 0.16$, which is a bit smaller than to Chariklo's adopted elongation (Table 1), making the points C_2 and C_4 unstable, see Main Text. Haumea's elongation $\epsilon = 0.61$ is well beyond the critical value, making C_2 and C_4 highly unstable.

Lindblad resonances

A particle revolving around the central body is submitted to a potential of generic form

$$U(\mathbf{r}) = \sum_{-\infty}^{+\infty} U_m(r) \cdot \cos(m\theta) = \sum_{-\infty}^{+\infty} U_m(r) \cdot \cos[m(L - \lambda_A)]. \quad (31)$$

The quantities r and L can be expressed in terms of the keplerian elements of the particle, a , e , λ and ϖ . In doing so, terms with frequency $j\kappa - m(n - \Omega)$ appear in the expansion of $U(\mathbf{r})$, where κ is the particle horizontal epicyclic frequency and j is a non negative integer. Each term for which

$$j\kappa \sim m(n - \Omega) \quad (j \text{ integer} > 0) \quad (32)$$

describes a resonance between the mean motion of the particle and the spin rate of the body. For bodies close to spherical, we have $\kappa \sim n$, and the condition above reads

$$\frac{n}{\Omega} \sim \frac{m}{m - j}, \quad (33)$$

referred to as an orbit-spin $m/(m - j)$ resonance. Its associated resonant critical angle is

$$\phi_{m,j} = [m\lambda_A - (m - j)\lambda - j\varpi]/j. \quad (34)$$

In the case of an ellipsoid, the potential (19) contains only even terms of the form $2p\theta$, so that the only resonances encountered have the form

$$\frac{n}{\Omega} \sim \frac{2p}{2p - j}. \quad (35)$$

The classical d'Alembert's rule implies that the term responsible for the $m/(m - j)$ resonance is of order e^j . Consequently, the strongest resonances are those with $j = 1$, and are classically referred to as Lindblad Eccentric Resonances, or simply Lindblad Resonances (LRs).

Note that we classically restrict the qualifier "Lindblad" to resonances of first order in e , i.e. of the form $\kappa = m(n - \Omega)$. Lindblad resonances of higher orders $k > 1$ are possible when they are forced by a satellite with eccentric orbit e_s . Then, the resonant term in the forcing potential is proportional to ee_s^{k-1} , i.e. still of first order in e , but of total order k in ee_s . In those cases, Ω must be replaced by a pattern speed Ω_{pat} that accounts for higher-order harmonics in the satellite motion³⁷. Those complications do not arise here because all the mass elements of the body execute circular motions around the center of mass.

The corresponding terms in the expansion of $U(\mathbf{r})$ are easily obtained by using the first order expansions, $r \approx a - ae \cos(\lambda - \varpi)$ and $L \approx \lambda + 2e \sin(\lambda - \varpi)$. Introducing them into $\sum_{-\infty}^{+\infty} U_m(r) \cdot \cos[m(L - \lambda_A)]$, we obtain to first order in eccentricity

$$U(\mathbf{r}) = \sum_{k=-\infty}^{+\infty} U_k(a) \cdot \cos[k(\lambda - \lambda_A)] - e \sum_{m=-\infty}^{+\infty} A_m(a) \cdot \cos(\phi_m), \quad (36)$$

where

$$\phi_m = m\lambda_A - (m-1)\lambda - \varpi \quad (37)$$

is the resonant angle associated with the $m/(m-1)$ LR and

$$A_m(a) = [2m + a(d/da)] U_m(a). \quad (38)$$

In order to separate the effects of the physical parameters of the body (Ω, R, q) and the effects of the resonances *per se*, we define a new dimensionless coefficient $\mathcal{A}_m = -(q/\Omega^2 R^2) A_m$, so that the potential can eventually be split into a corotation and a Lindblad resonance part,

$$U(\mathbf{r}) = \sum_{k=-\infty}^{+\infty} U_k(a) \cdot \cos[k(\lambda - \lambda_A)] + e \frac{\Omega^2 R^2}{q} \sum_{m=-\infty}^{+\infty} \mathcal{A}_m(a) \cdot \cos(\phi_m). \quad (39)$$

The coefficients \mathcal{A}_m are obtained from Eqs. 9, 19 and 38, and are listed in Supplementary Table 1. For large values of $|m|$, \mathcal{A}_m has the exponential behaviour $\mathcal{A}_m \propto K^{|m|}$ (K being a constant depending on the problem considered). Using Chariklo's parameters ($q = 0.226$), we obtain asymptotically that $\mathcal{A}_m \propto 0.54^{|m|} \mu \propto 0.54^{|m|} z^3$ in the mass anomaly case, and $\mathcal{A}_m \propto (1.93\epsilon q^{2/3})^{|m/2|} = (0.72\epsilon)^{|m/2|}$ in the ellipsoid case, using $q = 0.226$ (Chariklo case). Note that m is even in the latter case and that the $2/3$ LR is the strongest of all (Fig. 2), with $\mathcal{A}_{-2} \propto \epsilon$.

Choice of the friction coefficient η

Main Text Eq. (5) introduces a dimensionless friction coefficient η that quantifies the drag applied to the ring particles in our numerical integrations. Note that we do not consider any other forces acting on the particles, such as radiation pressure or Poynting-Roberston (PR) drag. This is justified by the fact that both Chariklo and Haumea's rings probably contain mainly cm- to m-sized particles, which are stable against PR drag over hundreds of millions years^{1,6}. This said, the choice of η is rather arbitrary as it does not enter in the expression of the torque Γ_m (Eq. (3)). However, it does define the typical width Δa_m of the $m/(m-1)$ LR, defined as the region over which most of the torque Γ_m is deposited around the resonance radius a_m . In order to be as realistic as possible about Δa_m , we choose the value of η to match the expected disk properties.

Following the formalism of ref. 20, the dimensionless width $\alpha = \Delta a_m/a_m$ of the resonance is determined by the dominant physical process at work in the disk, which can be self-gravity, viscosity or pressure. In the self gravity case, α is given by

$$\alpha_G = \sqrt{\frac{2\pi|m-1|G\Sigma_0}{3m^2\Omega^2 a_m}}, \quad (40)$$

where G is the gravitational constant and Σ_0 is the disk surface density. Using $\Sigma_0 = 500$ - 1000 kg m^{-2} (ref. 6), a rotation period of 7 h (Table 1), we obtain a typical value $\alpha_G \sim 2 \times 10^{-3}$.

If viscosity prevails, then α takes the form $\alpha_\nu = [7\nu/(9|m|\Omega a_m^2)]^{1/3} = [7/(9|m-1|)]^{1/3} (h/a_m)^{2/3}$. Taking $h \sim 10 \text{ m}$ and a typical $a_m \sim 250 \text{ km}$, we obtain $\alpha_\nu \lesssim 10^{-3}$, with similar values if the disk

is pressure-dominated. This shows that Chariklo's rings are likely to be dominated by self-gravity near LRs. Finally, the coefficient α associated with a Stokes-like force as in Main Text Eq. (5) is $\alpha_\eta = 2\eta/3|m|$, so that $\eta \sim 0.01$ provides a realistic estimation of the LR widths in Chariklo's rings, i.e. $\alpha_\eta \sim \alpha_G$. The same exercise can be performed for Haumea's rings, yielding smaller values of η , since both the spin rate Ω and the radii a_m are larger in this case. However, the orders of magnitude remain the same and the main conclusions of this work are not altered.

Higher order resonances

Besides the first order LRs considered in the Main Text (Eq. (2)), higher order $n/\Omega = m/(m-j)$ resonances appear, corresponding to $j > 1$ (as explained above, they are *not* Lindblad resonances). Being of order e^j , they are weaker than the LRs. Nevertheless, they may have significant effects in the ellipsoidal case, owing to the large values of Chariklo and Haumea's elongation parameters ϵ .

In that case, combining d'Alembert's rule and Eq. (19), we see that a $m/(m-j)$ resonance is of global order $e^j \epsilon^{|m/2|}$ (m even). For instance, while the outer 1/2 (first order) LR appears in the case of a mass anomaly, it only exists in its second order version 2/4 ($m = -2, j = 2$) in the case of the ellipsoid. Similarly, the outer 1/3 LR appears in its second order version with a mass anomaly, but only in its fourth order version 2/6 ($m = -2, j = 4$) when caused by an ellipsoid.

To our knowledge, no evaluation of the torque exerted at a $m/(m-j)$ resonance with $j > 1$ has been published. There are two reasons for that. First, the hydrodynamical equations describing the disk must be expanded to j^{th} order in the perturbations, a challenging task. Second, such resonances cause streamline self-crossings. It can be shown (Sicardy et al. 2018, in preparation) that near a $m/(m-j)$ resonance, where m and j are *relatively prime*, a periodic resonant streamline has j braids with $|m|(j-1)$ self-crossing points. This creates singularities in the hydrodynamical equations (shocks), even for vanishingly small perturbations, thus requiring new kinds of treatments.

This said, we see that although the 2/4 resonance (ellipsoid case) is of second order in the particle eccentricity, it does *not* induce self-crossing streamlines since the ratio 2/4 can be reduced to 1/2, resulting in $|-1|(1-1) = 0$ self-crossing points. Still, as mentioned above, no expression of the resonance torque exists because of the second-order nature of that resonance. A general behaviour can nevertheless be sketched. At second order in eccentricity, Eq. (39) is replaced by

$$U(\mathbf{r}) = \sum_{k=-\infty}^{+\infty} U_k(a) \cdot \cos[k(\lambda - \lambda_A)] + e^2 \frac{\Omega^2 R^2}{q} \sum_{m=-\infty}^{+\infty} \mathcal{B}_m(a) \cdot \cos(2\phi_m), \quad (41)$$

where now $\phi_m = [m\lambda_A - (m-2)\lambda - 2\varpi]/2$ (with m even). The expression of \mathcal{B}_m can be retrieved from ref. 37. It involves the operator

$$f_{45} = \frac{1}{8} \left[(4m^2 - 5m) + 2(2m-1)a \frac{d}{da} + a^2 \frac{d^2}{da^2} \right] \quad (42)$$

that must be applied to each term of the expansion given in Eq. (19). This provides

$$\mathcal{B}_m(a) = -\frac{1}{4} S_{|m/2|} \epsilon^{|m/2|} \left[(4m^2 - 5m) - 2(2m-1)(|m|+1) + (|m|+1)(|m|+2) \right] \left(\frac{R}{a} \right)^{|m|+1}, \quad (43)$$

which reduces to $\mathcal{B}_{-2} = -2.55(R/a_{1/2})^3\epsilon$, where $a_{1/2}$ is the radius of exact 2/4 resonance. The phase portrait of this resonance is found in various works (e.g. ref. 37). Posing $X = e \cos(\phi_{2/4})$ and $Y = e \sin(\phi_{2/4})$ ($\phi_{2/4} = 2\lambda - \lambda_A - \varpi$), it can be shown that the origin $(X, Y) = (0, 0)$ is always a fixed point. It is stable, except for a narrow interval of initial semi-major axes $a_{1/2}(1 - 0.25\epsilon) \lesssim a \lesssim a_{1/2}(1 + 0.25\epsilon)$, the coefficient ~ 0.25 stemming from the particular values of R and q used here. In that interval (of width ~ 25 km for Chariklo and ~ 375 km for Haumea, from Main Text Table 1), the origin $(X, Y) = (0, 0)$ is an unstable hyperbolic point, so that ring particles initially orbiting on those circular orbits periodically acquire orbital eccentricities of order $e \sim \sqrt{0.25\epsilon}$. This shows that a Chariklo with elongation $\epsilon \sim 0.20$ forces large excentricities ($e \sim 0.2$) at the second-order 2/4 resonance (see an example in Supplementary Fig. 2), while Haumea $\epsilon \sim 0.61$ forces even larger values ($e \sim 0.35$) that lead to collisions with the body. The 2/4 resonant zone is thus a highly perturbed region where no ring is expected to survive.

Turning to the second order 1/3 (mass anomaly) and fourth order 2/6 (ellipsoid) resonances, we see that it is the unique prograde resonant orbit with only one self-crossing point (corresponding to $m = -1$ and $j = 2$, so that $|m|(j - 1) = 1$). Our numerical integrations show no significant effect of the 2/6 resonance on the particle motion, even with an elongation as high as $\epsilon = 0.61$ (Haumea's case). This stems from the fourth-order nature of that resonance. It is noteworthy that both Chariklo and Haumea's rings are close to the 1/3 resonance configuration^{2, 12}, possibly leading to yet-to-be explicated more subtle confining effects of a narrow ring at that location. This makes further investigations (in particular using collisional codes) highly desirable.

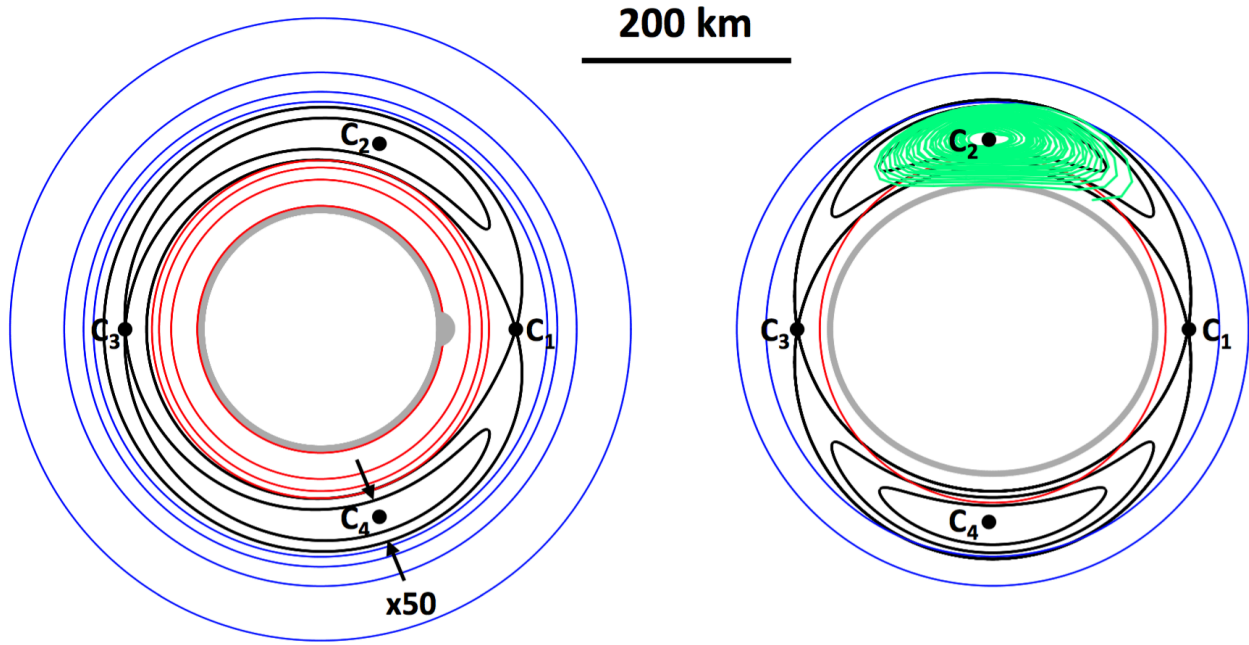


Figure 1

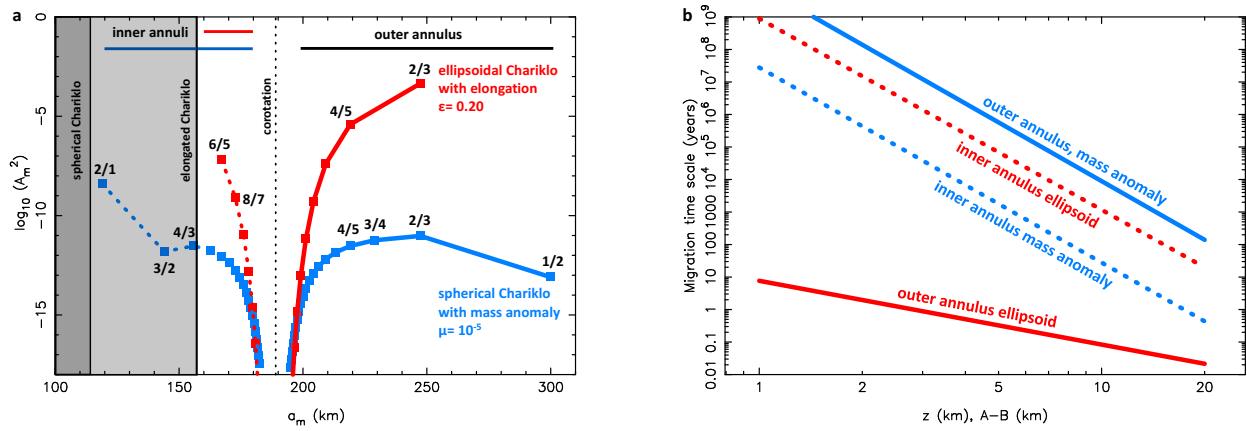


Figure 2

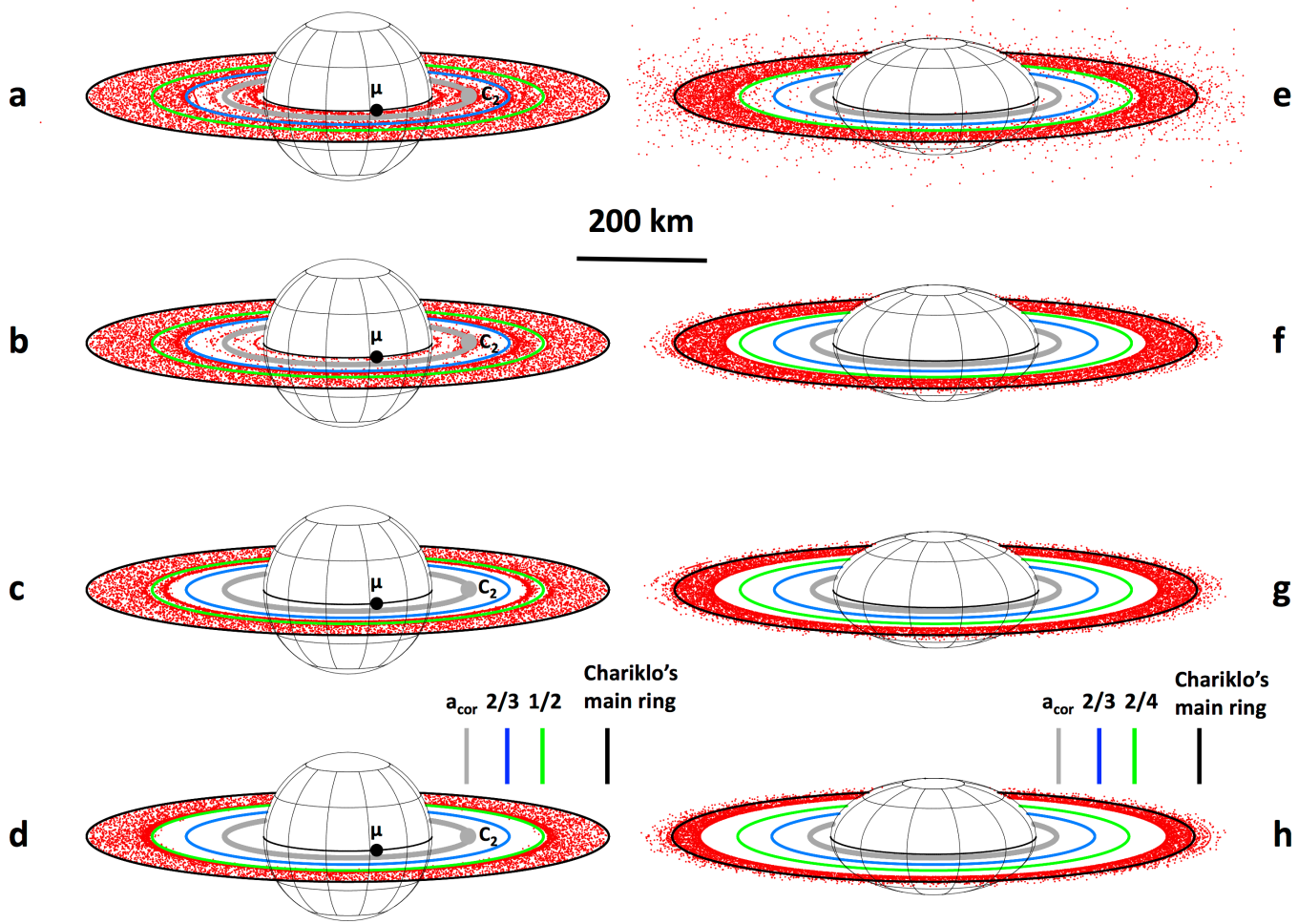


Figure 3

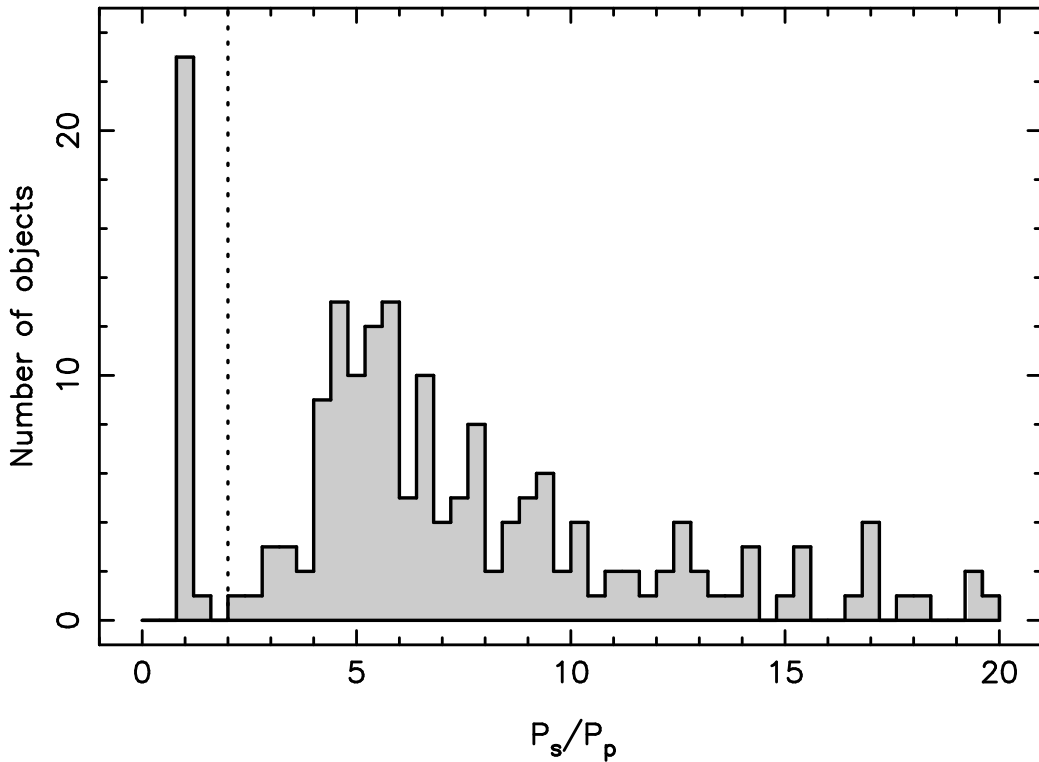
Supplementary Table 1:

Azimuthal variation $f(\theta)$ of the corotation potential (Methods Eq. (26))	
Mass anomaly	$q^{-1/6} \left(\frac{1}{\sqrt{q^{1/3} + q^{-1/3} - 2 \cos \theta}} - q^{1/2} \cos \theta \right) \cdot \mu$
Triaxial ellipsoid ^(a)	$2 \sum_{p=1}^{+\infty} q^{2p/3} S_p \epsilon^p \cos(2p\theta)$
Coefficients $\mathcal{A}_m(a)$ of the $m/(m-1)$ Lindblad resonances (Main Text Eq. (3) and Methods Eq. (39))	
Mass anomaly ^(b)	$\left\{ \left[m + \frac{a}{2} \frac{d}{da} \right] b_{1/2}^{(m)}(a/R_{\text{sph}}) + q \left(\frac{a}{2R_{\text{sph}}} \right) \delta_{(m,-1)} \right\} \cdot \mu$
Triaxial ellipsoid ^(e) (with m even)	$[2m - (m + 1)] S_{ m/2 } \left(\frac{R}{a} \right)^{ m +1} \cdot \epsilon^{ m/2 }$

(a) The sequence S_p is defined by Eq. (20).

(b) Assuming a spherical body of radius R_{sph} . The terms $b_{1/2}^{(m)}$ are the Laplace coefficients and $\delta_{(m,-1)}$ is the Kronecker delta function.

Supplementary Figure 1:



Supplementary Figure 2:

